

Linearly-polarized Coherent Emission from Relativistic Magnetized Ion-electron Shocks

Masanori Iwamoto,^{1,2,*} Yosuke Matsumoto,³ Takanobu Amano,⁴ Shuichi Matsukiyo,² and Masahiro Hoshino⁴

¹*Yukawa Institute for Theoretical Physics, Kyoto University,
Kitashirakawa-Oiwakecho, Sakyo-Ku, Kyoto 606-8502, Japan*

²*Faculty of Engineering Sciences, Kyushu University,
6-1, Kasuga-koen, Kasuga, Fukuoka, 816-8580, Japan*

³*Institute for Advanced Academic Research, Chiba University,
1-33 Yayoi, Inage-ku, Chiba, Chiba 263-8522, Japan*

⁴*Department of Earth and Planetary Science, University of Tokyo,
7-3-1 Hongo, Bunkyo-ku, Tokyo 113-0033, Japan*

Fast radio bursts (FRBs) are millisecond transient astrophysical phenomena and bright at radio frequencies. The emission mechanism, however, remains unsolved yet. One scenario is a coherent emission associated with the magnetar flares and resulting relativistic shock waves. Here, we report unprecedentedly large-scale simulations of relativistic magnetized ion-electron shocks, showing that strongly linear-polarized electromagnetic waves are excited. The kinetic energy conversion to the emission is so efficient that the wave amplitude is responsible for the brightness. We also find a polarization angle swing reflecting shock front modulation, implicating the polarization property of some repeating FRBs. The results support the shock scenario as an origin of the FRBs.

Fast radio bursts (FRBs) are luminous millisecond-duration pulses detected at radio frequencies near 1 gigahertz (GHz) mostly from extragalactic origins [1, 2]. Some FRBs are known to repeat, while most of them do not. The mechanism powering the non-repeating FRBs remains a topic of debate [3, 4]. On the other hand, magnetars are often invoked for the progenitor of the repeating FRBs [5], which is supported by the recent discovery of FRB 200428 associated with a galactic magnetar [6, 7]. The extremely high brightness temperature of FRBs requires coherent emission in the sense that electron bunches collectively emit electromagnetic waves [8]. One of the promising coherent emission mechanisms is synchrotron maser instability (SMI) in relativistic magnetized shocks induced by the magnetar flares [9–14]. The fundamental properties of the SMI have been studied by using ab-initio Particle-in-Cell (PIC) simulations and have been confirmed that the coherent emission is intrinsic to relativistic magnetized shocks [15–24]. The SMI in the context of relativistic magnetized shocks can self-consistently convert the incoming flare energies into coherent emission.

The observed rotation measure of some repeating FRBs indicates the magneto-ionic environments of the sources [25], and thus relativistic magnetized shocks can be induced in baryon-loaded shells [12–14]. Although the SMI model usually assumes the energy conversion ratio from incoming total energy into electromagnetic wave energy $f_\xi \sim 10^{-3}$, which was confirmed by PIC simulations of pair (electron-positron) shocks [21–23], f_ξ in ion-electron shocks remains unclear especially in realistic three-dimensional (3D) systems. The observational fact that repeating FRBs often exhibit the high degree of linear polarization [26–30] constrains the emission mechanism as well. Previous 2D PIC simulations

demonstrate the excitation of the two linearly polarized waves: extraordinary (X) and ordinary (O) mode waves [22, 31, 32]. 3D shock simulations are required for properly taking into account the both X and O mode wave contribution to the polarization. In this Letter, we demonstrate that $f_\xi \sim 10^{-3}$ is indeed satisfied and determine the precise state of the polarization based on the Stokes parameter analysis. Our unprecedentedly large-scale PIC simulations of 3D ion-electron shocks reveal the underlying physical process of the SMI-induced coherent emission and provide the detailed description of the wave properties.

We quantify the emission efficiency and polarization properties of the coherent emission by using a fully kinetic electromagnetic PIC code, which enables long-term stable calculations of a relativistic plasma flow [33–35]. The Japanese flagship supercomputer Fugaku at the RIKEN Center for Computational Science helps us to perform 3D ion-electron shock simulations. The unit of length is the electron skin depth c/ω_{pe} , which is the characteristic electron kinetic scale and resolved with 20 computational cells. The simulation time step is set as $0.05\omega_{pe}^{-1}$. In the above expression, c is the speed of light and $\omega_{pe} = \sqrt{4\pi N_1 e^2 / \gamma_1 m_e}$ is the relativistic electron plasma frequency with the upstream electron number density N_1 and bulk Lorentz factor of the upstream plasma flow γ_1 . The computational domain is a square prism with $0 \leq x/(c/\omega_{pe}) \leq 2000$, $0 \leq y/(c/\omega_{pe}) \leq 46$, and $0 \leq z/(c/\omega_{pe}) \leq 46$ for $\sigma_i = 0.1$ and $0 \leq x/(c/\omega_{pe}) \leq 2000$, $0 \leq y/(c/\omega_{pe}) \leq 23$, and $0 \leq z/(c/\omega_{pe}) \leq 23$ for $\sigma_i = 0.5$, where $\sigma_i = B_1^2 / 4\pi\gamma_1 N_1 m_i c^2$ is the ion magnetization parameter and $\mathbf{B}_1 = (0, 0, B_1)$ is the upstream background magnetic field. The periodic boundary condition is applied in the y and z directions for both particles and fields. The lower x boundary at $x = 0$ is the

conducting wall. A cold ion-electron plasma flow drifting in the $-x$ direction are continuously injected from the upper x boundary. The interaction between the injected and reflected plasma flow triggers shocks propagating the $+x$ direction, and thus the simulation frame corresponds to the downstream rest frame. We examine the two cases $\sigma_i = 0.1$ and 0.5 , which are motivated by the SMI model [12–14]. The ion-to-electron mass ratio is fixed as $m_i/m_e = 200$ throughout this study. Note that the electron magnetization parameter $\sigma_e = m_i\sigma_i/m_e = 20$ and 100 is satisfied and electrons are highly magnetized. We consider the highly relativistic plasma flow with $\gamma_1 = 40$. The number of particles per electron skin depth per species in the upstream is set as $N_1(c/\omega_{pe})^3 = 32000$. The transverse box size is comparable to the upstream ion gyro-radius, which is sufficiently large to capture essential physical processes reported by previous 2D simulations under different parameters and configurations [21, 22, 36].

Figure 1 shows the snapshots for $\sigma_i = 0.1$ (left) and 0.5 (right) at the final state of our simulations $\omega_{pe}t = 2000$. All physical quantities are normalized by the corresponding upstream ones. The ion number density N_i (top) is strongly modified in the upstream region due to the filamentation instability (FI). The FI is a transverse self-modulation of an electromagnetic wave [37–41] and the density filaments are also observed in the previous simulations of 2D ion-electron shock [31, 32, 36]. N_i for relatively high magnetization $\sigma_i = 0.5$ exhibits sheet-like structures perpendicular to the ambient magnetic field rather than filamentary structures, which is consistent with the previous simulations of 3D pair shocks with high magnetization [24]. This is probably because the magnetic pressure dominates over the ponderomotive force for high magnetization and particles are preferentially pushed along the ambient magnetic field [37, 38]. The magnetic field B_z (bottom) show large-amplitude electromagnetic waves are excited by the SMI. Since the ponderomotive force exerted by the electromagnetic waves induces the FI, the FI gets weaker as the wave amplitude gets smaller [40, 41]. As will be shown later, the radiant power for $\sigma_i = 0.5$ is smaller than that for $\sigma_i = 0.1$. Therefore, the FI for $\sigma_i = 0.5$ is relatively weak and the wave propagation is not strongly disturbed. We thus think that the electromagnetic waves for $\sigma_i = 0.5$ are mostly planar. The filamentary structures corresponding to the density filaments are seen for $\sigma_i = 0.1$. The electromagnetic waves are accumulated in the low density region $N_i/N_1 < 1$, indicating that the dispersion measure of FRBs can be modified [40]. The fluctuation of the inferred dispersion measure [42] can be attributed to the FI via the SMI.

The energy conversion ratio f_ξ is quantified as a function of total magnetization $\sigma_{tot} = \sigma_i/(1 + m_e/m_i) \simeq \sigma_i$ in the downstream rest frame and shown in Figure 2 with circles. The conversion ratios from the incoming total en-

ergy to the X mode, O mode, total (i.e., X+O) wave energies are shown in red, green, and, blue, respectively. We determine f_ξ in the upstream region $1400 \leq x/(c/\omega_{pe}) \leq 1700$ for $\sigma_i = 0.5$ and $1000 \leq x/(c/\omega_{pe}) \leq 1300$ for $\sigma_i = 0.1$ at $\omega_{pe}t = 2000$. The X mode wave amplitude is systematically larger than the O mode wave because the O mode waves are induced by the magnetic field fluctuations along the ambient magnetic field due to the Alfvén ion cyclotron instability (AIC) which are suppressed for high magnetization [22]. Note that the linear theory of the SMI predicts only the X mode wave excitation [16]. Present results show that the assumption $f_\xi \sim 10^{-3}$ is valid even for 3D ion-electron shocks. The black dashed line indicates the previous simulation results of 2D pair shocks [22]. Note that the emission efficiency in pair shocks can be twice as high as ion-electron shocks because both electrons and positrons contribute to the electromagnetic wave emission via the SMI. The emission efficiency of 2D pair shocks is almost comparable to that of 3D ion-electron shocks due to the ion-electron coupling [36, 43, 44]. Since f_ξ in pair shocks remains unchanged in 2D and 3D for $\sigma_{tot} \gtrsim 0.1$ [23, 24], this tendency holds for 3D. For $\sigma_{tot} \gg 1$, however, the previous studies in pair shocks show $f_\xi \sim 10^{-3}/\sigma_{tot}$, and thus the emission efficiency disfavors the SMI in highly magnetized shocks. The intense electromagnetic waves excite wakefields (i.e., electrostatic plasma waves) via stimulated Raman scattering in the upstream region. Then, the wakefields accelerate the incoming electrons and take the kinetic energy from the ion flow. The accelerated electrons provide more energy to the SMI and the emission efficiency is enhanced. The stronger wakefields are in turn excited, completing the feedback loop. This loop continues until the energy equipartition between electrons and ions is achieved in the upstream region. Although electrons transfer only a small fraction of the incoming kinetic energy, the SMI can indirectly consume the ion kinetic energy and thus σ_{tot} controls the emission efficiency. This ion-electron coupling can work for highly relativistic shocks $\gamma_1 \gg 1$. For mildly relativistic shocks (i.e., γ_1 is the order of unity), the amplitude of the wakefield is too small to accelerate the incoming electrons and the upstream electron kinetic energy is almost constant. Therefore, the ion-electron coupling does not work and the SMI in mildly relativistic shocks becomes less efficient [31, 32]. Since the SMI model generally considers highly relativistic shocks, the ion-electron coupling operates and the assumption $f_\xi \sim 10^{-3}$ is valid in terms of γ_1 as well.

The degree of linear polarization (DOLP) is shown in the top panel of Figure 3 for $\sigma_i = 0.1$ (red) and $\sigma_i = 0.5$ (blue). We perform Fourier transform of fluctuating magnetic fields along the line of sight (x direction in our coordinates) in the same region as f_ξ and calculate the DOLP from the Stokes parameters [45]: I, Q, U and V averaged over the transverse direction. The wave power spec-

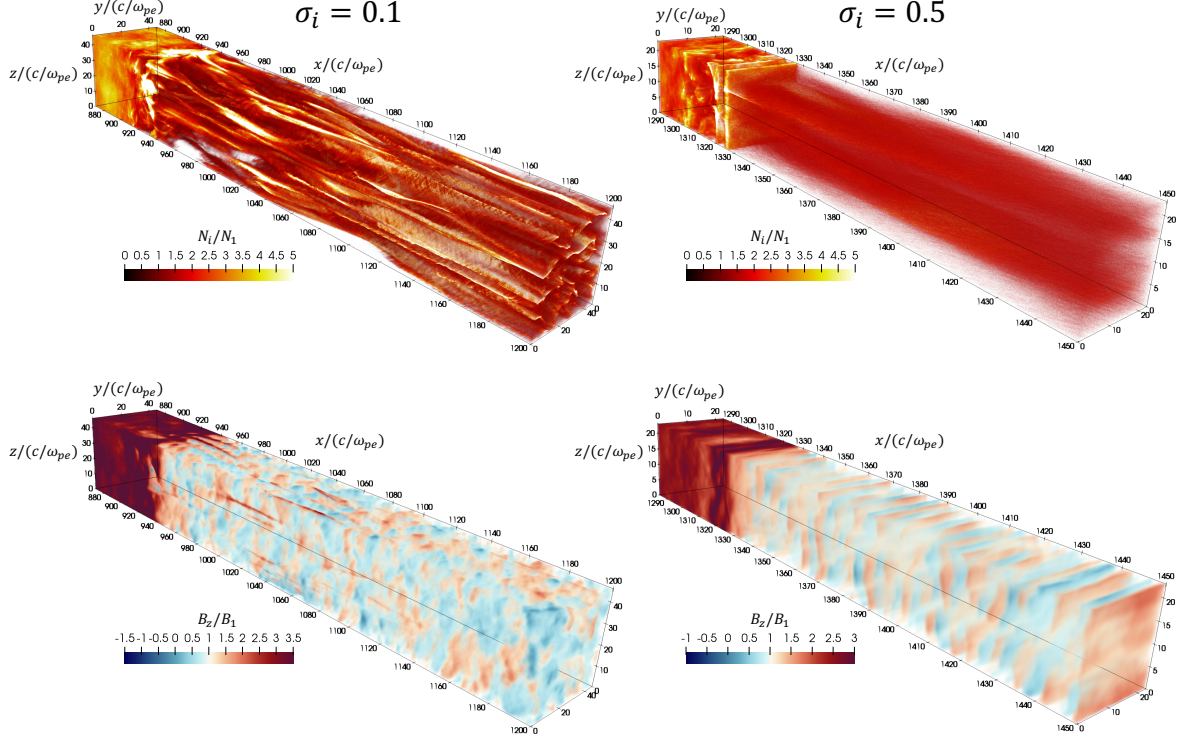


FIG. 1. Global structures of relativistic magnetized shocks. The ion number density (top) and z components of magnetic field (bottom) at the final state $\omega_{pe}t = 2000$ are shown for $\sigma_i = 0.1$ (left) and 0.5 (right). The color scales for the two cases of σ_i are the same.

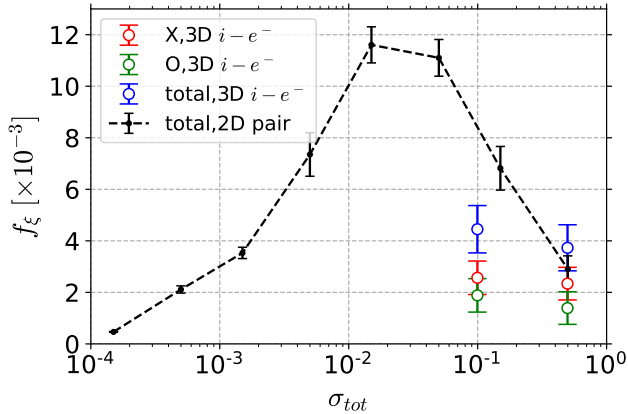


FIG. 2. Energy conversion ratios as a function of total magnetization determined from the snapshots at the final state $\omega_{pe}t = 2000$. The X, O, total waves are shown in red, green, and blue circles, respectively. The black dashed line indicates the total power measured in previous 2D pair shock simulations for comparison [22].

tra of X (solid lines) and O (dashed lines) mode waves $\delta\mathbf{B} = \mathbf{B} - \mathbf{B}_1$ integrated over the transverse wavevector k_y and k_z are shown in the bottom panel. The peak

of the power spectra at $ck_x/\omega_{pe} \sim 0$ comes from the FI because the low-wavenumber waves $ck_x/\omega_{pe} \sim 0$ cannot escape upstream and the fluctuations must be induced by the FI in the upstream rather than the SMI in the shock transition [21–23]. Previous simulations of pair shocks [18, 21–23] show the wave power takes the maximum at $ck_x/\omega_{pe} \sim 3 - 5$, which is obviously larger than the ion-electron shocks. This can be explained by the ion-electron coupling. The upstream bulk Lorentz factor for electrons becomes $\gamma_{eff} \sim m_i\gamma_1/2m_e$ due to the energy equipartition and the upstream electron plasma frequency decreases by a factor of $\sqrt{m_i/2m_e} = 10$, resulting in the peak shift [5]. The cutoff wavenumber below which the electromagnetic waves cannot catch up with the shocks also decreases, and thus a sharp cutoff is not observed unlike pair shocks. For $\sigma_i = 0.1$, the DOLP is 60% at $ck_x/\omega_{pe} \sim 0.2$ where the X-mode wave power takes the maximum. For $\sigma_i = 0.5$, the electromagnetic waves are more highly linearly polarized for the wide range of the wavenumber and the DOLP is higher than 60% at around the peak $ck_x/\omega_{pe} \sim 0.8$. Furthermore, it reaches almost 100% at $ck_x/\omega_{pe} \sim 0.2$ where the electromagnetic waves still have significant power. We determine the accurate DOLP of the synchrotron maser emission based on Stokes parameters and show for the

first time that it is considerably high at the dominant modes.

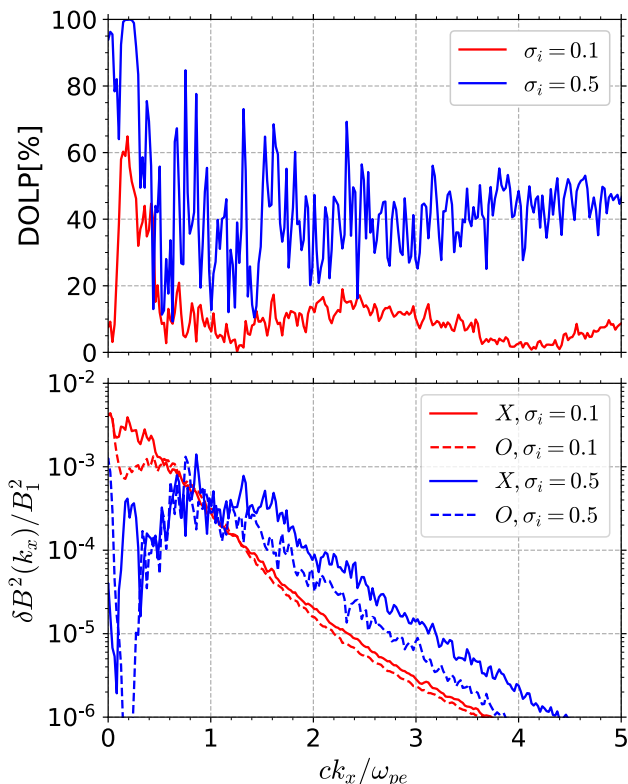


FIG. 3. Degree of linear polarization (DOLP) and wave power spectra along the line of sight at the final state $\omega_{pe}t = 2000$. The red and blue indicates $\sigma_i = 0.1$ and 0.5 , respectively. DOLP (top) is calculated from transversely-averaged Stokes parameters. Power spectra of X (solid lines) and O (dashed lines) mode waves are shown in the bottom panel.

The polarization angle (PA) of the synchrotron maser emission is no longer constant due to the excitation of the O mode wave. The PA in units of degree is determined for the electromagnetic waves that have been emitted at the early phase of the shock evolution: $1750 \leq x/(c/\omega_{pe}) \leq 1950$ and shown in Figure 4 for $\sigma_i = 0.1$ (red) and 0.5 (blue). We determine Stokes parameters along the line of sight (x direction) with the spatial window width $10c/\omega_{pe}$. The PA along the line of sight is calculated from them at each position and then averaged over both transverse direction and wavenumber space. The error bars are determined from the standard deviation of the PA. For both σ_i , the PA is almost constant in the region $1900 \leq x/(c/\omega_{pe}) \leq 1950$ because only the X mode waves are generated at the early phase of the shock evolution. The O mode waves are induced when the ambient magnetic field is sufficiently perturbed by the AIC, and thus the O mode waves lag behind the X mode waves [31, 36]. Note that the group velocities of these two waves are almost equal to the speed of light

and the time delay of arrival comes from the difference of excitation time. In the region $x/(c/\omega_{pe}) \leq 1900$, the PA is strongly modified and the errors become larger due to the mixture of the X and O mode waves. Especially for $\sigma_i = 0.5$, the PA drastically changes and this change can be observed as the PA swing. Since both X and O mode waves are induced in pair shocks as well [22, 24], the PA swing can be observed regardless of the plasma components. The observations of FRB 180301 indeed show the various PA swings, and this observational fact is believed to be an indirect proof that FRBs originate from the coherent curvature emission of electron bunches formed in the magnetar magnetosphere [29]. However, our simulations indicate that the PA swings can be reproduced also by the synchrotron maser emission and the mixture of the two different linearly polarized waves can result in the diversity of the PA.

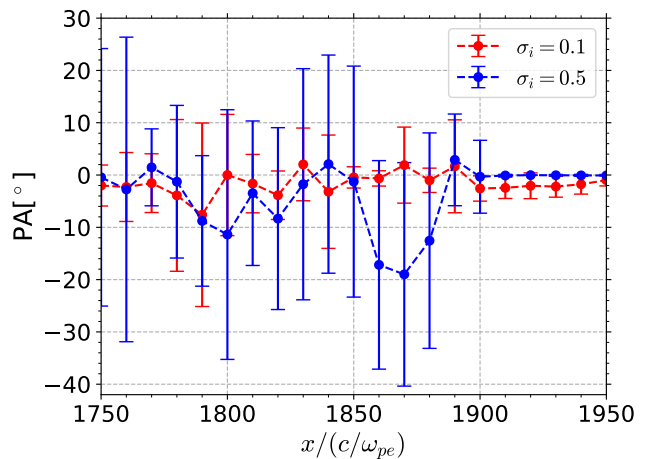


FIG. 4. Polarization angle (PA) along the line of sight at the final state $\omega_{pe}t = 2000$. The red and blue lines represent $\sigma_i = 0.1$ and 0.5 , respectively. PA is calculated from transversely-averaged Stokes parameters with the spatial window width $10c/\omega_{pe}$.

We now discuss the peak frequency of the synchrotron maser emission based on the previous work [23]. The peak wavenumber in the downstream rest frame k_{peak} can be expressed as (see the bottom panel in Figure 3)

$$k_{peak} \sim \zeta \sqrt{\frac{2m_e \omega_{pe}}{m_i c}}, \quad (1)$$

where ζ is a few. The factor $\sqrt{2m_e/m_i}$ comes from the ion-electron coupling [5]. Since the dispersion relation of the electromagnetic waves in the downstream rest frame is written as $\omega^2 = \omega_{pe}^2 + c^2 k^2$ for $\sigma_e/\gamma_1^2 \gg 1$ [31], the peak frequency in the upstream rest frame ν_{peak} is

$$\nu_{peak} \sim \gamma_1 \sqrt{1 + \zeta^2} \sqrt{\frac{2m_e \omega_{pe}}{m_i} \frac{1}{2\pi}} \sim 1\text{GHz} \sqrt{\frac{\gamma_{sh}^2 n_0}{10^{13}\text{cm}^{-3}}}, \quad (2)$$

where γ_{sh} and n_0 are the shock Lorentz factor and the upstream electron number density measured in the upstream rest frame, respectively. Here we have used $\gamma_1 \sim \gamma_{sh}$, which is valid for $\sigma_i \leq 1$, and neglected factors of order of unity. If the upstream rest frame corresponds to the observer frame, which is the case for the baryon-loaded shell expanding with the non-relativistic speed, $\gamma_{sh}^2 n_0 \sim 10^{13} \text{cm}^{-3}$ is required for the coherent emission in GHz band. The SMI model [12–14] can satisfy the condition for a reasonable choice of parameters. The obtained emission efficiency f_ξ may change if the upstream plasmas are hot [46]. Even though the upstream plasmas are initially cold, the FI and the stimulated Raman scattering lead to the heating and even to the generation of the nonthermal particles in the upstream [36, 47]. The temperature dependence of the emission efficiency f_ξ in ion-electron shocks remains unsolved. Inclusion of positrons may affect the emission efficiency as well. In ion-electron-positron plasmas, the resonant interaction between the incoming positrons and ions via the SMI occurs in the shock transition and a significant fraction of the ion kinetic energy is preferentially transferred to the positrons [16, 17]. Furthermore, wakefields become weaker because both electrons and positrons are pushed by the ponderomotive force, and the ion-electron coupling in the upstream region can be inefficient. The emission efficiency in ion-electron-positron shocks is still an open question.

We are grateful to Lorenzo Sironi, Emanuele Sobacchi, Jacek Niemiec, and Martin Pohl for fruitful discussions. This research was supported by MEXT as “Program for Promoting Researches on the Supercomputer Fugaku” (Toward a unified view of the universe: from large scale structures to planets, JPMXP1020200109) and JICFuS. MI acknowledges support from JSPS KAKENHI grant No. 20J00280, 20KK0064 and 22H00130.

* masanori.iwamoto@yukawa.kyoto-u.ac.jp

- [1] D. R. Lorimer, M. Bailes, M. A. McLaughlin, D. J. Narkevic, and F. Crawford, A Bright Millisecond Radio Burst of Extragalactic Origin, *Science* **318**, 777 (2007).
- [2] E. Petroff, J. W. Hessels, and D. R. Lorimer, Fast radio bursts at the dawn of the 2020s, *Astron. Astrophys. Rev.* **30**, 1 (2022).
- [3] J. I. Katz, The sources of apparently non-repeating FRB, *Mon. Not. R. Astron. Soc.* **516**, 53 (2022).
- [4] S. Bhandari, A. C. Gordon, D. R. Scott, L. Marnoch, N. Sridhar, P. Kumar, C. W. James, H. Qiu, K. W. Bannister, A. T. Deller, T. Eftekhari, W.-f. Fong, M. Glowacki, J. X. Prochaska, S. D. Ryder, R. M. Shannon, and S. Simha, A Nonrepeating Fast Radio Burst in a Dwarf Host Galaxy, *Astrophys. J.* **948**, 67 (2023).
- [5] Y. Lyubarsky, Emission Mechanisms of Fast Radio Bursts, *Universe* **7**, 56 (2021).
- [6] B. C. Andersen, K. M. Bandura, M. Bhardwaj, A. Bij, M. M. Boyce, P. J. Boyle, C. Brar, T. Cassanelli, P. Chawla, T. Chen, J. F. Cliche, A. Cook, D. Cubranic, A. P. Curtin, N. T. Denman, M. Dobbs, F. Q. Dong, M. Fandino, E. Fonseca, B. M. Gaensler, U. Giri, D. C. Good, M. Halpern, A. S. Hill, G. F. Hinshaw, C. Höfer, A. Josephy, J. W. Kania, V. M. Kaspi, T. L. Landecker, C. Leung, D. Z. Li, H. H. Lin, K. W. Masui, R. Mckinven, J. Mena-Parra, M. Merryfield, B. W. Meyers, D. Michilli, N. Milutinovic, A. Mirhosseini, M. Münchmeyer, A. Naidu, L. B. Newburgh, C. Ng, C. Patel, U. L. Pen, T. Pinsonneault-Marotte, Z. Pleunis, B. M. Quine, M. Rafiei-Ravandi, M. Rahman, S. M. Ransom, A. Renard, P. Sanghavi, P. Scholz, J. R. Shaw, K. Shin, S. R. Siegel, S. Singh, R. J. Smegal, K. M. Smith, I. H. Stairs, C. M. Tan, S. P. Tendulkar, I. Tretyakov, K. Vanderlinde, H. Wang, D. Wulf, and A. V. Zwaniga, A bright millisecond-duration radio burst from a Galactic magnetar, *Nature* **587**, 54 (2020).
- [7] C. D. Bochenek, V. Ravi, K. V. Belov, G. Hallinan, J. Kocz, S. R. Kulkarni, and D. L. McKenna, A fast radio burst associated with a Galactic magnetar, *Nature* **587**, 59 (2020).
- [8] J. I. Katz, Coherent emission in fast radio bursts, *Phys. Rev. D* **89**, 103009 (2014).
- [9] Y. Lyubarsky, A model for fast extragalactic radio bursts, *Mon. Not. R. Astron. Soc.* **442**, L9 (2014).
- [10] A. M. Beloborodov, A Flaring Magnetar in FRB 121102?, *Astrophys. J.* **843**, L26 (2017).
- [11] A. M. Beloborodov, Blast Waves from Magnetar Flares and Fast Radio Bursts, *Astrophys. J.* **896**, 142 (2020).
- [12] B. D. Metzger, B. Margalit, and L. Sironi, Fast radio bursts as synchrotron maser emission from decelerating relativistic blast waves, *Mon. Notices Royal Astron. Soc.* **485**, 4091 (2019).
- [13] B. Margalit, B. D. Metzger, and L. Sironi, Constraints on the engines of fast radio bursts, *Mon. Not. R. Astron. Soc.* **494**, 4627 (2020).
- [14] B. Margalit, P. Beniamini, N. Sridhar, and B. D. Metzger, Implications of a “Fast Radio Burst” from a Galactic Magnetar, *Astrophys. J. Lett.* **899**, L27 (2020).
- [15] A. B. Langdon, J. Arons, and C. E. Max, Structure of Relativistic Magnetosonic Shocks in Electron-Positron Plasmas, *Phys. Rev. Lett.* **61**, 779 (1988).
- [16] M. Hoshino and J. Arons, Preferential positron heating and acceleration by synchrotron maser instabilities in relativistic positron–electron–proton plasmas, *Phys. Fluids B* **3**, 818 (1991).
- [17] M. Hoshino, J. Arons, Y. A. Gallant, and A. B. Langdon, Relativistic magnetosonic shock waves in synchrotron sources - Shock structure and nonthermal acceleration of positrons, *Astrophys. J.* **390**, 454 (1992).
- [18] Y. A. Gallant, M. Hoshino, A. B. Langdon, J. Arons, and C. E. Max, Relativistic, perpendicular shocks in electron-positron plasmas, *Astrophys. J.* **391**, 73 (1992).
- [19] E. Amato and J. Arons, Heating and nonthermal particle acceleration in relativistic, transverse magnetosonic shock waves in proton-electron-positron plasmas, *Astrophys. J.* **653**, 325 (2006).
- [20] L. Sironi and A. Spitkovsky, PARTICLE ACCELERATION IN RELATIVISTIC MAGNETIZED COLLISIONLESS ELECTRON-ION SHOCKS, *Astrophys. J.* **726**, 75 (2011).
- [21] M. Iwamoto, T. Amano, M. Hoshino, and Y. Matsumoto, Persistence of Precursor Waves in Two-dimensional Rel-

- ativistic Shocks, *Astrophys. J.* **840**, 52 (2017).
- [22] M. Iwamoto, T. Amano, M. Hoshino, and Y. Matsumoto, Precursor Wave Emission Enhanced by Weibel Instability in Relativistic Shocks, *Astrophys. J.* **858**, 93 (2018).
- [23] I. Plotnikov and L. Sironi, The synchrotron maser emission from relativistic shocks in Fast Radio Bursts: 1D PIC simulations of cold pair plasmas, *Mon. Not. R. Astron. Soc.* **485**, 3816 (2019).
- [24] L. Sironi, I. Plotnikov, J. Nättilä, and A. M. Beloborodov, Coherent Electromagnetic Emission from Relativistic Magnetized Shocks, *Phys. Rev. Lett.* **127**, 035101 (2021).
- [25] R. Mckinven, B. M. Gaensler, D. Michilli, K. Masui, V. M. Kaspi, J. Su, M. Bhardwaj, T. Cassanelli, P. Chawla, F. A. Dong, E. Fonseca, C. Leung, D. Z. Li, C. Ng, C. Patel, A. B. Pearlman, E. Petroff, Z. Pleunis, M. Raffei-Ravandi, M. Rahman, K. R. Sand, K. Shin, I. H. Stairs, and S. Tendulkar, Revealing the Dynamic Magnetoionic Environments of Repeating Fast Radio Burst Sources through Multiyear Polarimetric Monitoring with CHIME/FRB, *Astrophys. J.* **951**, 82 (2023).
- [26] K. Masui, H. H. Lin, J. Sievers, C. J. Anderson, T. C. Chang, X. Chen, A. Ganguly, M. Jarvis, C. Y. Kuo, Y. C. Li, Y. W. Liao, M. McLaughlin, U. L. Pen, J. B. Peterson, A. Roman, P. T. Timbie, T. Voytek, and J. K. Yadav, Dense magnetized plasma associated with a fast radio burst, *Nature* **528**, 523 (2015).
- [27] D. Michilli, A. Seymour, J. W. Hessels, L. G. Spitler, V. Gajjar, A. M. Archibald, G. C. Bower, S. Chatterjee, J. M. Cordes, K. Gourdji, G. H. Heald, V. M. Kaspi, C. J. Law, C. Sobey, E. A. Adams, C. G. Bassa, S. Bogdanov, C. Brinkman, P. Demorest, F. Fernandez, G. Hellbourg, T. J. Lazio, R. S. Lynch, N. Maddox, B. Marcote, M. A. McLaughlin, Z. Paragi, S. M. Ransom, P. Scholz, A. P. Siemion, S. P. Tendulkar, P. Van Rooy, R. S. Wharton, and D. Whitlow, An extreme magneto-ionic environment associated with the fast radio burst source FRB 121102, *Nature* **553**, 182 (2018).
- [28] E. Petroff, J. W. T. Hessels, and D. R. Lorimer, Fast radio bursts, *Astron. Astrophys. Rev.* **27**, 4 (2019).
- [29] R. Luo, B. J. Wang, Y. P. Men, C. F. Zhang, J. C. Jiang, H. Xu, W. Y. Wang, K. J. Lee, J. L. Han, B. Zhang, R. N. Caballero, M. Z. Chen, X. L. Chen, H. Q. Gan, Y. J. Guo, L. F. Hao, Y. X. Huang, P. Jiang, H. Li, J. Li, Z. X. Li, J. T. Luo, J. Pan, X. Pei, L. Qian, J. H. Sun, M. Wang, N. Wang, Z. G. Wen, R. X. Xu, Y. H. Xu, J. Yan, W. M. Yan, D. J. Yu, J. P. Yuan, S. B. Zhang, and Y. Zhu, Diverse polarization angle swings from a repeating fast radio burst source, *Nature* **586**, 693 (2020).
- [30] C. K. Day, A. T. Deller, R. M. Shannon, H. Qiu, K. W. Bannister, S. Bhandari, R. Ekers, C. Flynn, C. W. James, J.-P. Macquart, E. K. Mahony, C. J. Phillips, and J. Xavier Prochaska, High time resolution and polarization properties of ASKAP-localized fast radio bursts, *Mon. Not. R. Astron. Soc.* **497**, 3335 (2020).
- [31] A. Ligorini, J. Niemiec, O. Kobzar, M. Iwamoto, A. Bohdan, M. Pohl, Y. Matsumoto, T. Amano, S. Matsukiyo, Y. Esaki, and M. Hoshino, Mildly relativistic magnetized shocks in electron–ion plasmas – I. Electromagnetic shock structure, *Mon. Not. R. Astron. Soc.* **501**, 4837 (2021).
- [32] A. Ligorini, J. Niemiec, O. Kobzar, M. Iwamoto, A. Bohdan, M. Pohl, Y. Matsumoto, T. Amano, S. Matsukiyo, and M. Hoshino, Mildly relativistic magnetized shocks in electron–ion plasmas – II. Particle acceleration and heating, *Mon. Not. R. Astron. Soc.* **502**, 5065 (2021).
- [33] Y. Matsumoto, T. Amano, T. N. Kato, and M. Hoshino, Stochastic electron acceleration during spontaneous turbulent reconnection in a strong shock wave, *Science* **347**, 974 (2015).
- [34] Y. Matsumoto, T. Amano, T. N. Kato, and M. Hoshino, Electron Surfing and Drift Accelerations in a Weibel-Dominated High-Mach-Number Shock, *Phys. Rev. Lett.* **119**, 105101 (2017).
- [35] N. Ikeya and Y. Matsumoto, Stability property of numerical Cherenkov radiation and its application to relativistic shock simulations, *Publ. Astron. Soc. Jpn.* **67**, 64 (2015).
- [36] M. Iwamoto, T. Amano, M. Hoshino, Y. Matsumoto, J. Niemiec, A. Ligorini, O. Kobzar, and M. Pohl, Precursor Wave Amplification by Ion–Electron Coupling through Wakefield in Relativistic Shocks, *Astrophys. J. Lett.* **883**, L35 (2019).
- [37] E. Sobacchi, Y. Lyubarsky, A. M. Beloborodov, and L. Sironi, Self-modulation of fast radio bursts, *Mon. Not. R. Astron. Soc.* **500**, 272 (2020).
- [38] E. Sobacchi, Y. Lyubarsky, A. M. Beloborodov, and L. Sironi, Filamentation of fast radio bursts in magnetar winds, *Mon. Not. R. Astron. Soc.* **511**, 4766 (2022).
- [39] A. Ghosh, D. Kagan, U. Keshet, and Y. Lyubarsky, Non-linear Electromagnetic-wave Interactions in Pair Plasma. I. Nonrelativistic Regime, *Astrophys. J.* **930**, 106 (2022).
- [40] E. Sobacchi, Y. Lyubarsky, A. M. Beloborodov, L. Sironi, and M. Iwamoto, Saturation of the Filamentation Instability and Dispersion Measure of Fast Radio Bursts, *Astrophys. J. Lett.* **943**, L21 (2023).
- [41] M. Iwamoto, E. Sobacchi, and L. Sironi, Kinetic simulations of the filamentation instability in pair plasmas, *Mon. Not. R. Astron. Soc.* **522**, 2133 (2023).
- [42] J. I. Katz, The environment and constraints on the mass of FRB 190520B, *Mon. Not. R. Astron. Soc.* **514**, L27 (2022).
- [43] Y. Lyubarsky, Electron-Ion Coupling Upstream of Relativistic Collisionless Shocks, *Astrophys. J.* **652**, 1297 (2006).
- [44] M. Hoshino, Wakefield Acceleration by Radiation Pressure in Relativistic Shock Waves, *Astrophys. J.* **672**, 940 (2008).
- [45] G. B. Rybicki and A. D. Lightman, *Radiative Processes in Astrophysics* (John Wiley & Sons, Inc., New York, 1979).
- [46] A.-N. Babul and L. Sironi, The synchrotron maser emission from relativistic magnetized shocks: dependence on the pre-shock temperature, *Mon. Not. R. Astron. Soc.* **499**, 2884 (2020).
- [47] M. Iwamoto, T. Amano, Y. Matsumoto, S. Matsukiyo, and M. Hoshino, Particle Acceleration by Pickup Process Upstream of Relativistic Shocks, *Astrophys. J.* **924**, 108 (2022).